Electrical conductivity tensor of β-Ga$_2$O$_3$ analyzed by van der Pauw measurements: Inherent anisotropy, off-diagonal element, and the impact of grain boundaries

Christian Golz,[1] Zbigniew Galazka,[2] Jonas Lähnemann,[3] Vanesa Hortelano,[1] Fariba Hatami,[1]
W. Ted Masselink,[1] and Oliver Bierwagen[3,*]

[1]*Department of Physics, Humboldt-Universität zu Berlin, Newton-Strasse 15, D-12489 Berlin, Germany*
[2]*Leibniz-Institut für Kristallzüchtung, Max-Born-Strasse 2, D-12489 Berlin, Germany*
[3]*Paul-Drude-Institut für Festkörperelektronik, Leibniz-Institut im Forschungsverbund Berlin e.V.,*
Hausvogteiplatz 5–7, D-10117 Berlin, Germany

The semiconducting oxide β-gallium oxide (β-Ga$_2$O$_3$) possesses a monoclinic unit cell, whose low symmetry generally leads to anisotropic physical properties. For example, its electrical conductivity is generally described by a polar symmetrical tensor of second rank consisting of four independent components. Using van der Pauw measurements in a well-defined square geometry on differently oriented high-quality bulk samples and the comparison to finite-element simulations, we precisely determine the ratio of all elements of the β-Ga$_2$O$_3$ three-dimensional electrical conductivity tensor. Despite the strong structural anisotropy, a weakly anisotropic conductivity at and above room temperature was found. In the a^*bc coordinate system, the diagonal elements deviate from each other by no more than 6%. Based on these results and the off-diagonal element being $\approx$5% of the diagonal ones, the direction of highest conductivity is rotated $(59 \pm 15)^\circ$ from the c direction towards the a^* direction with a conductivity of $(1.12 \pm 0.09)\times$ that in the perpendicular direction of lowest conductivity. Analysis of the temperature dependence of the anisotropy and mobility of differently doped samples allows us to compare the anisotropy for dominant phonon scattering to that for dominant ionized-impurity scattering. For both scattering mechanisms, the conductivities along the a and b direction agree within 2%. In contrast, the conductivity along the c direction amounts to $0.96\times$ that along the b direction for dominant phonon scattering, and up to $1.12\times$ for ionized-impurity scattering. The transport anisotropies are determined to be larger than the theoretically predicted effective mass anisotropy, suggesting slightly anisotropic scattering mechanisms. We demonstrate that significantly higher anisotropies can be caused by oriented, extended structural defects in the form of low-angle grain boundaries, for which we determined energy barriers of up to 93 meV.

I. INTRODUCTION

β-Ga$_2$O$_3$, the thermodynamically stable polymorph of solid Ga$_2$O$_3$, is a promising material for several applications such as high-power electronics [1,2] and deep UV photodetectors [2,3], and it can be used for high-temperature gas sensors [4]. β-Ga$_2$O$_3$ has a monoclinic lattice structure, which corresponds to the $C2/m$ space group with lattice parameters of $a = 12.23$ Å, $b = 3.04$ Å, and $c = 5.80$ Å and an angle of 103.7° between the a and c axes [5]. Due to this angle, the basis vectors of the unit cell, a and c, are not orthogonal to the (100) and (001) planes in β-Ga$_2$O$_3$, respectively. The low symmetry of the unit cell is prone to result in anisotropic physical properties.

Notable anisotropies in β-Ga$_2$O$_3$ have been found in the thermal conductivity [6–8] as well as the dielectric function by the polarization-dependent refractive index [9] and fundamental onset of optical absorption [9–11]. In addition, slight anisotropies of the high-frequency and static dielectric constant of β-Ga$_2$O$_3$ have been reported by theory and experiment [12–16].

The conductivity anisotropy is given by the ratio of the electrical conductivity in two different defined directions. The same holds true for the mobility tensor $\bar{\mu}$, as the conductivity tensor $\bar{\sigma} = en\bar{\mu}$, with the charge carrier density n and electronic charge e being scalars.

For electronic device applications such as transistors, a mobility anisotropy would translate into an increased performance of the devices oriented along a certain crystallographic direction compared to those along other directions. As shown in Table I, quite contradictory experimental values on the conductivity anisotropy can be found in the literature, whereas no estimate has been reported so far on the off-diagonal element of conductivity. Reported conductivity anisotropies range from 17-times-higher conductivity for the b direction compared to the c direction [10], over the same mobility in the a and b directions, and 1.2-times-higher conductivity in the c direction [20] to a negligible anisotropy [17], where no direction was favored for transport. In metal-oxide-semiconductor field-effect transistors (MOSFETs), a 10–15% larger channel mobility in the a^* direction compared to the c direction has been observed [21]. Using ellipsometry, the same mobility

*bierwagen@pdi-berlin.de

TABLE I. Overview of the literature on transport anisotropies and associated methods in β-Ga$_2$O$_3$. The "Anisotropy" is the "Quantity" in direction "Dir. 1" divided by that in "Dir. 2" at room-temperature electron concentration "n@RT." Directions a, b, c are parallel to the a, b, c axes of the unit cell, and a^*, c^* are parallel to the (100), (001) surface normals. "n/s" denotes "not specified." †: The anisotropy of less than 1.1 for σ (line 3) was calculated from a van der Pauw resistance anisotropy ratio of less than 1.3 given in Ref. [17] using the conversion into conductivity anisotropy elaborated in Ref. [18]. #: The samples used for different transport directions (line 4) had different electron concentrations.

Quantity	Method	Dir. 1	Dir. 2	Anisotropy	n(cm^{-3}) @RT	Ref.
σ	4-probe	b	c	17 (extrinsic)	5.2×10^{18}	[10]
σ	van der Pauw	b	c	2 (twins)	$>10^{18}$	[19]
σ	van der Pauw	all	all	<1.1 †	5×10^{16}–5×10^{17}	[17]
μ	Hall bar	c	a, b	1.2 #	$4 \times 10^{17}, 7 \times 10^{17}, 9 \times 10^{17}$	[20]
μ	MOSFET channel	a^*	c	1.1	3×10^{17}	[21]
μ	ellipsometry	a, b	c^*	2	3.5×10^{18}	[14]
μ	optical Hall	all	all	<1.1	$4 \times 10^{18}, 6 \times 10^{18}$	[22]
μ_{PLOPS}	theory	c^*	a	1.18 to 1.40	10^{17} to 10^{20}	[23]
μ_{PLOPS}	theory	a	b	0.85 to 0.78	10^{17} to 10^{20}	[23]
μ_{PLOPS}	theory	c^*	b	1.01 to 1.09	10^{17} to 10^{20}	[23]
μ_{IIS}	theory	n/s	n/s	estimated <1.4		[23]
μ_{PLOPS}	theory	c^*	b	0.64 to 0.92	5×10^{17} to 10^{19}	[24]
μ_{IIS}	theory	any	any	assumed 1	5×10^{17} to 10^{19}	[24]
$\mu_{\mathrm{PLOPS+IIS}}$	theory	c^*	b	0.69 to 0.92	5×10^{17} to 10^{19}	[24]
m^*	optical Hall	all	all	<1.1	$4 \times 10^{18}, 6 \times 10^{18}$	[22]
m^*	theory	all	all	<1.05		[12,25–27]

in a and b, but only half the mobility in the c direction, has been measured [14]. In combination with an external magnetic field, the same method, termed optical Hall effect, has yielded rather isotropic mobilities (within $\approx$10%) [22].

As the mobility depends on the effective mass m^* and scattering time τ, $\mu = \frac{e\tau}{m^*}$, its anisotropy is determined by the anisotropy of m^* and τ. First-principles calculations from several groups using different methods arrive at a fairly isotropic effective electron mass [12,25–27] with anisotropies typically below 1.05, which is confirmed by experimental data of the effective mass using optical Hall effect measurements [22].

The scattering time is related to the dominant scattering mechanism, polar longitudinal optical-phonon scattering (PLOPS), and ionized impurity scattering (IIS) [23,24,28]. At and above room temperature, the mobility is typically limited by PLOPS [23,28], whereas IIS is dominating at high impurity or point-defect densities (including compensating impurities/point defects) or lower temperatures. Depending on the scattering mechanism, the monoclinic symmetry of β-Ga$_2$O$_3$ suggests more or less anisotropic scattering times. Hence, the change of dominant scattering mechanism with temperature likely leads to a temperature-dependent anisotropy of the scattering rates. Recent first-principles calculations of the electron mobility limit of β-Ga$_2$O$_3$, indeed, suggested a moderate anisotropy with higher mobility in the c^* than in the a or b directions [23]. In that work, the PLOPS-limited mobility (neglecting IIS) in the c^* direction has been predicted to be up to 9% and 40% higher than in the a and b directions, respectively, to become more isotropic with decreasing electron concentrations, and anisotropies of up to 1.4 for the IIS-limited mobility were estimated. Another first-principles study [24] predicts opposite trends for the PLOPS-limited mobility with a 36% lower mobility in the c^* than in the b direction, which becomes

more isotropic with increasing electron concentration, and isotropic IIS.

Besides the intrinsic material properties, samples might be extrinsically anisotropic on average due to oriented extended defects such as grain boundaries and twin boundaries. As an example, Ref. [19] found a room-temperature transport anisotropy as high as 2 in Ga$_2$O$_3$(100) thin films containing a high density of incoherent twin boundaries. Likewise, the high anisotropy of 17 from Ref. [10] has been interpreted in terms of extrinsic causes by Refs. [17,23].

In this paper, we experimentally determine the intrinsic anisotropy and relative magnitude of the off-diagonal element of the conductivity tensor of β-Ga$_2$O$_3$ with high accuracy (uncertainty of <5%) to shed light on the conflicting values of published theoretical and experimental transport anisotropy. The extracted conductivity is close to isotropic and we demonstrate large transport anisotropies to be extrinsically caused by extended defects.

II. SAMPLES AND METHOD

A. Samples

To largely rule out the extrinsic effect of extended defects on transport anisotropy, semiconducting bulk substrates were chosen as the sample material with the highest structural quality available. Square-shaped 5×5 mm^2 (0.5 to 0.7 mm thickness) wafers with different orientations, i.e., Czochralski-grown [29,30] (100), (001), and ($\bar{2}$01) as well as edge-defined film fed grown [31] ($\bar{2}$01) and (010) (from Tamura Corporation) were investigated in this work. The edges of the squares were oriented along low-index crystallographic directions. The samples are described in Table II. Samples G100a1–a2, G001a1–a3, and G-201a were prepared from the same boule grown by the Czochralski method at the Leibniz-Institut für

TABLE II. Overview of the results of the x-ray diffraction measurements and the properties of the samples: orientation, doping, room-temperature Hall electron density and mobility, and assessed quality. The surface orientation is given by the numbers in the sample name. UID refers to unintentionally doped samples.

Sample name	Orientation; Edges	Doping	Electron density (cm^{-3})	Electron mobility (cm^2/Vs)	Quality	XRD ω reflection	ω rocking curve FWHM (°)
G100a1	(1 0 0); [0 1 0], [0 0 1]	UID	2.9×10^{17}	123	high	(4 0 0)	0.060
G100a2	(1 0 0); [0 1 0], [0 0 1]	UID	2.5×10^{17}	125	high	(4 0 0)	0.012
G100b	(1 0 0); [0 1 0], [0 0 1]	UID	8.3×10^{16}	60	high	(4 0 0)	0.041
G100c	(1 0 0); [0 1 0], [0 0 1]	UID	5.6×10^{17}	104	low (extended defects)	(4 0 0)	~2
G001a1	(0 0 1); [1 0 0], [0 1 0]	UID	4.7×10^{17}	111	high	(0 0 2)	0.015
G001a2	(0 0 1); [1 0 0], [0 1 0]	UID	3.9×10^{17}	120	high	(0 0 2)	0.022
G001a3	(0 0 1); [1 0 0], [0 1 0]	UID	3.0×10^{17}	134	high	(0 0 2)	0.020
G-201a	($\bar{2}$ 0 1); [1 0 2], [0 1 0]	UID	4.7×10^{17}	111	high	($\bar{2}$ 0 1)	0.017
G-201at1	($\bar{2}$ 0 1); [1 0 2], [0 1 0]	UID	1.3×10^{17}	156	high	($\bar{2}$ 0 1)	0.016
G-201at2	($\bar{2}$ 0 1); [1 0 2], [0 1 0]	UID	1.3×10^{17}	156	high	($\bar{2}$ 0 1)	0.016
G-201bt	($\bar{2}$ 0 1); [1 0 2], [0 1 0]	Sn	5.9×10^{18}	69	high	($\bar{2}$ 0 1)	0.034
G010at	(0 1 0); [1 0 2], ($\bar{2}$ 0 1)	UID	1.1×10^{17}	125	high	(0 2 0)	0.012
G010bt	(0 1 0); [1 0 2], ($\bar{2}$ 0 1)	Sn	1.3×10^{18}	65	high	(0 2 0)	0.029

Kristallzüchtung. To study the impact of extended defects on the transport anisotropy, a (100)-oriented sample containing low-angle grain boundaries, G100c, was prepared.

Disk-shaped ohmic contacts of 100 to 300 μm diameter close to the corners of the sample were reproducibly defined on the top surface of the samples using photolithography to minimize geometrical errors. A distance of the contacts from the sample edges of 700 to 850 μm was chosen to prevent unintentionally contacting the side of the sample by individual contacts. This approach ensures reproducible and well-defined current injection (only through the top surface) by all four contacts to provide a current distribution that can be readily compared to the results of our corresponding finite-element calculations. All contacts were deposited by electron beam evaporation of Ti/Pt/Au (20/20/150 nm), followed by rapid thermal annealing at 480 °C for 60 s in N_2. The Pt layer served as the diffusion barrier as deterioration of Ti/Au contacts was observed upon annealing.

The electron densities of the samples were in the range of 8×10^{16} to 6×10^{18} cm^{-3} at room temperature.

B. Structural characterization

The crystal quality of the wafers was assessed by x-ray diffraction (XRD) using Cu-Kα radiation and a 1 mm detector slit. Wide-range, symmetric, on-axis $2\Theta - \omega$ scans confirmed phase-pure material by the presence of only the β-Ga_2O_3 reflexes belonging to the specified wafer orientation. Figure 1(a) shows an example for the two (100)-oriented wafers G100a2 and G100c. To detect the potential existence of twins or rotational domains, off-axis XRD peaks were measured by Φ scans with rotational angle Φ around the surface normal. In these scans, the off-axis diffraction peaks were measured in skew-symmetric geometry with the sample tilted by the angle Ψ. The presence of a single peak in the Φ scan of the 4 0 1 reflex for all (1 0 0)- and (0 0 1)-oriented samples, exemplarily shown in Fig. 1(b) for G100a2 and G100c, confirms the absence of twins or rotational domains. Likewise, a onefold rotational symmetry was confirmed for all (-2 0 1)-oriented samples by the presence of only one peak in the Φ scan of the

4 0 0 reflex (not shown), and the expected twofold rotational symmetry was confirmed for all (0 1 0)-oriented samples by the presence of only two peaks, 180° apart from each other, in the Φ scan of the 1 1 1 reflex (not shown).

To assess the crystal quality in more detail, ω-rocking curves of the on-axis substrate reflections, sensitive to lattice tilting, were taken for all samples. The low full width at half maximum of these curves below 0.1°, documented in Table II, confirms the comparably high crystalline quality. The only exception is sample G100c, with a rocking curve consisting of a broad distribution of narrow peaks, whose origin is discussed next.

Low-angle grain boundaries in G100c

Figure 2 compares this sample to two other (1 0 0)-oriented ones. Photographs of the wafers placed between two crossed polarizers with white-light illumination from the backside exhibit a comparably homogeneous contrast for G100b, shown in Fig. 2(a), but an inhomogeneous contrast with stripes oriented approximately along the [0 1 0] direction
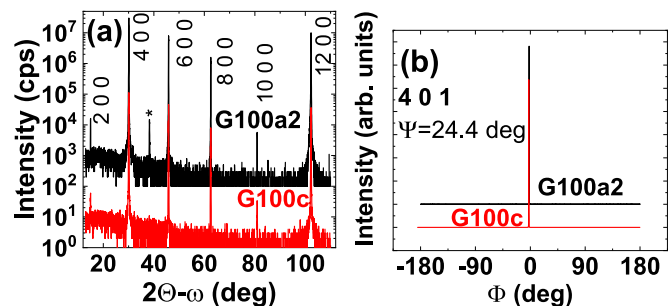

FIG. 1. XRD scans to determine the substrate orientation shown exemplarily for samples G100a2 and G100c. (a) Symmetric on-axis $2\Theta - \omega$ scans showing the presence of reflexes, labeled by their Miller indices, only related to the 1 0 0 wafer orientation. The peak marked by "*" is related to Au(1 1 1) of the ohmic contact. (b) ϕ scan of the 4 0 1 reflex. The onefold rotational symmetry indicates a single-crystalline material without rotational domains or twins.
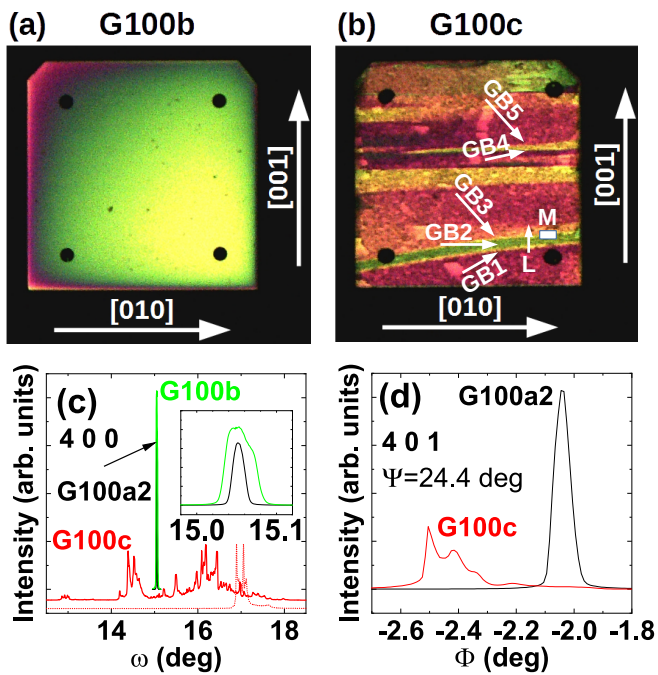
FIG. 2. Comparison of (100)-oriented wafers with different structural quality: G100a2, b without and G100c with low-angle grain boundaries. (a),(b) Photographs of (a) G100b and (b) G100c placed between two crossed polarizers with white-light illumination from the backside. The crystallographic directions are indicated by white arrows. Horizontal lines in the sample G100c indicate the grain boundaries. No such defects are visible in the sample G100b. The dark dots are the disk-shaped ohmic contacts. White arrows and labels on the wafer in (b) mark the positions of EBSD scans of grain boundaries shown in Fig. 3. (c) XRD ω-rocking curves of the 4 0 0 reflex of samples G100a2, b, and c, with the inset detailing those of G100a2 and b. The solid (dotted) red line describes the tilt mosaic of G100c towards the [0 1 0] ([0 0 1]) direction. (d) XRD detailed Φ scan of the 4 0 1 reflex of G100a2 and G100c.

for G100c, shown in Fig. 2(b). These stripes likely represent single-crystalline domains that are slightly twisted and tilted with respect to each other, as indicated by the multipeak structure of the rocking curve [Fig. 2(c)] and detailed Φ scan [Fig. 2(d)], respectively. The inhomogeneous contrast is due to the trichroism of β-Ga_2O_3 resulting in differently colored regions for differently oriented grains.

To clarify the nature of the grain boundaries, scanning electron microscopy (SEM)-based electron backscatter diffraction (EBSD) maps and line scans of the surface were taken for sample G100c. While XRD results give an integral picture of the orientation of single-crystalline domains, EBSD provides related local information on the orientation [32]. Figure 3(a) shows an EBSD map of the orientation deviation for a representative low-angle grain boundary in the region marked "M" in Fig. 2(b). The average misorientation between the two grains is about 2.2°. Variations within the individual grains are due to the limited accuracy chosen for this map. To resolve the misorientations for the different rotation axes and achieve a higher accuracy, we have resorted to high-resolution (HR)-EBSD measurements based on the cross correlation of high-quality Kikuchi patterns [33] using the commercial
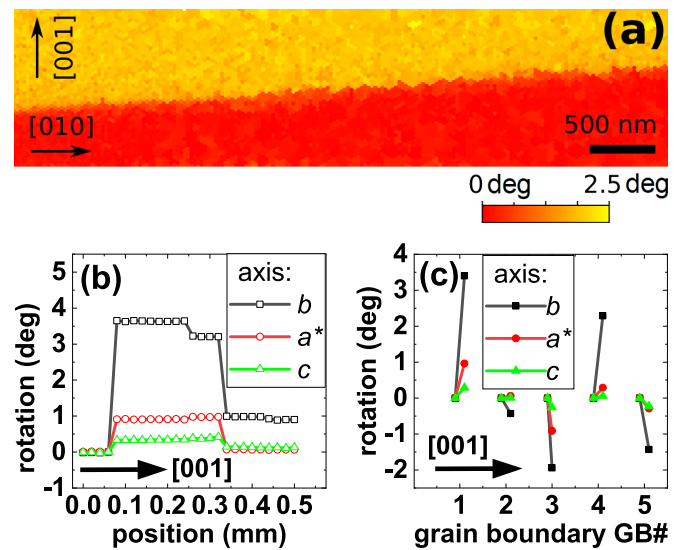

FIG. 3. Local variations of the surface orientation measured by EBSD for the G100c sample. (a) Map of the orientation deviation around the grain boundary marked "M" in Fig. 2(b) with the overall rotation angle relative to the average orientation of the lower grain encoded on a color scale. (b) HR-EBSD line scan with a step size of 20 μm crossing three grain boundaries along the (vertical) arrow "L" in Fig. 2(b). The deviation is given by the individual rotation angles around the specified axes. (c) Relative misorientation between adjacent grains extracted from microscopic line scans across the grain boundaries marked by "GBx" in Fig. 2(b). GB1–3 correspond to the boundaries in (b).

tool CROSS-COURT3. Figure 3(b) depicts a "macroscopic" HR-EBSD line scan [marked by "L" in Fig. 2(b)] across three low-angle grain boundaries achieved by mechanically shifting the sample stage and recording Kikuchi patterns at each position. Additionally, the relative rotations obtained from microscopic line scans across five grain boundaries [marked GB1–GB5 in Fig. 2(b)] are summarized in Fig. 3(c). These measurements show that the misorientation at the grain boundaries is dominated by a rotation around the b axis of up to 3.6°, i.e., the main rotation axis lies in the plane of the sample and is orientated along the grain boundary. The rotation around the out-of-plane a^* axis can be up to 1°, while the c axis shows only minor contributions of less than 0.3°. These local measurements of the rotation are consistent with the global data provided by the ω-rocking curves for sample G100c.

Hence, all investigated wafers can be considered single crystalline, except for G100c, which consists of a finite number of single-crystalline domains with low-angle (<4°) grain boundaries. This sample allows us to investigate the influence of low-angle grain boundaries on the transport properties.

C. Extracting a two-dimensional conductivity anisotropy by van der Pauw measurements and simulation

In order to investigate the effect of the scattering mechanisms and energy barriers due to low-angle grain boundaries on the conductivity anisotropy, transport measurements were conducted. These measurements were done in van der Pauw
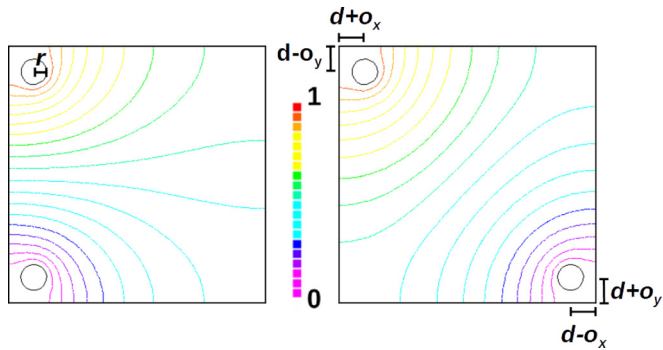
FIG. 4. Potential distribution calculated by finite element simulation of a square shaped van der Pauw sample in the configuration used for resistivity anisotropy measurements (left) and Hall-effect measurements (right). r denotes contact radius, d is the distance from the contact to the edge, and o_x and o_y are the offset of the contact position in these directions. This image was calculated for isotropic conductivity, no magnetic field and a geometry relative to the sample length defined by r, d, o_x, and o_y, being 0.05, 0.1, 0, and 0.

TABLE III. Van der Pauw resistance anisotropy A_{vdP} calculated by two-dimensional FEM simulations for square samples with conductivity anisotropy A and different sizes and positions (offset o_x as shown in Fig. 4) of the disk-shaped contacts. All sizes are relative to the edge length of the square sample. Note that for isotropic conductivity and symmetric contact placement, the van der Pauw anisotropy is unity for all values of the contact radius and distance of the contacts from the edge.

Contact radius	Distance contact to the edge	Offset of contact position o_x	A	A_{vdP}
All values	All values	0	1	1
0.05	0.2	0.1	1	1.14
0.01	0.01	0	1.1	1.35
0.05	0.1	0	1.1	1.32
0.05	0.2	0	1.1	1.26
0.01	0.01	0	2	9.4
0.05	0.1	0	2	7.7
0.05	0.2	0	2	5.4

geometry (square with four contacts close to the corners) at temperatures between 50 and 380 K in a closed-cycle helium refrigerator.

Hall measurements were performed in a magnetic field of $B = \pm 0.5$ T, oriented perpendicular to the substrate surface. For Hall measurements, the two sets of contacts diagonal to each other are used for applying current I and measuring voltage V, respectively. Using the two contacts on one edge parallel to x of the square sample for applying I and those on the opposite edge for measuring V, the four-terminal resistance along x, R_x, is determined. The same is done for the other two edges (perpendicular to the former ones), which yields R_y. These R_x and R_y are used as described in the original work by van der Pauw to calculate the geometrical average of the anisotropic sheet resistance $R_{ave} = 1/\sqrt{\sigma_x \sigma_y}$, with sheet conductivities σ_x and σ_y in the x and y direction, respectively. The van der Pauw resistance anisotropy is given by their ratio $A_{vdP} = R_y/R_x$. This value can be translated into the conductivity anisotropy $A = \sigma_x/\sigma_y$ along these axes using finite-element method (FEM) simulations of the current and voltage distribution for each sample.

We recently described in detail how we used this method for the determination of the transport anisotropy of another semiconducting oxide with anisotropic crystal structure, SnO_2 [34], and compared the method to the Hall bar geometry [18]. In addition, we have demonstrated the validity of the anisotropic van der Pauw method for the conductivity anisotropy due to a finite number of oriented planar defects by FEM simulations in the Supplemental Material of [34].

For each sample, geometric details were derived from micrograph images, including the size, position, and shape of the contacts. Using our FEM simulations, the impact of deviations from the ideal van der Pauw geometry for each sample (such as extended size and position of the contacts away from the sample edges) on measured sheet resistance, its anisotropy, as well as electron concentration n and resulting average mobility $\mu_{ave} = \sqrt{\mu_x \mu_y}$ are correctly accounted for. Examples of a potential distribution resulting from the FEM simulation can be found in Fig. 4. The relation $A(A_{vdP})$ and

correction factors for R_{ave}, n, μ_{ave} derived from FEM simulations for the geometries used in this work are summarized in Tables III and IV, respectively, as well as in Ref. [34].

Obtaining reliable values of A crucially depends on a precisely defined contact geometry as any deviation from a square arrangement by an aspect ratio L_x/L_y of a sample with a length of L_x and L_y impacts the resulting conductivity (or mobility) anisotropy A by a factor $(L_x/L_y)^2$ [18]. We tested the accuracy of our experimental technique using several isotropic Si bulk samples, a highly perfect semiconductor, and contact geometry defined by photolithography. The resulting deviations of A from unity were $<0.7\%$ for each of these samples, which can be seen as the intrinsic geometrical uncertainty of our experiment. A potential experimental artifact that can impact the observed in-plane conductivity anisotropy is the microscopic location of the current injection into the semiconductor under the ohmic contact pad. In our simulations, we are assuming current injection along the periphery of the contact. Low electron concentrations and low temperatures can, however, lead to a significant increase of contact resistance and inhomogeneous current injection underneath the contacts

TABLE IV. Correction factors for quantities derived from van der Pauw and Hall measurements for square samples with different sizes and positions (offset o_x as shown in Fig. 4) of the disk-shaped contacts, calculated using two-dimensional FEM simulations. Measured quantities are multiplied by the correction F to obtain the "true" quantities. All sizes are relative to the edge length of the square sample.

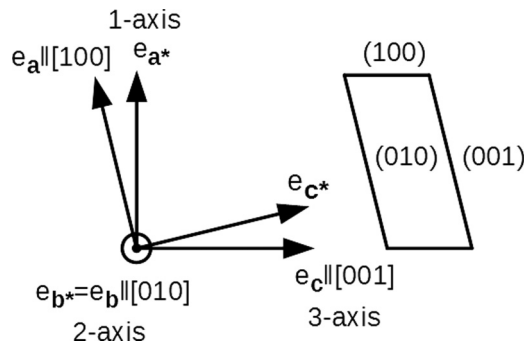| Contact radius	Distance contacts to the edge	Offset of contact position o_x	F for R_{ave}	F for n	F for μ_{ave}
0	0	0	1	1	1
0.05	0.1	0	1.01	0.84	1.18
0.05	0.2	0	1.10	0.58	1.57
0.01	0.15	0	1.02	0.80	1.23
0.05	0.2	0.1	1.09	0.60	1.53

FIG. 5. The unit cell of β-Ga$_2$O$_3$ projected along the b axis (= [010] direction). The unit basis vectors along the directions a, b, c and the unit vectors perpendicular to the (100), (010), (001) planes (along a^*, b^*, and c^*) are shown. The 1-axis=e_a^*, 2-axis=e_b, and 3-axis=e_c refer to the chosen Cartesian coordinate system to describe the conductivity tensor in this work (a^*bc system). The angle between a^* and a as well as c and c^* is 13.7°. The directions a, a^*, c, c^* are in the shown plane and perpendicular to $b = b^*$.

(contact freeze-out). For the lithographically defined contacts with diameter of 300 (100) μm, whose center has a distance of 850 (750) μm to the nearest sample edges, a maximum anisotropy artifact can arise for current injection only at one point on the contact pad that is located, e.g., in the horizontal direction towards the outer edge of the sample, but in the vertical direction towards the center of the sample. In this extreme case, the maximum apparent van der Pauw anisotropy for isotropic conductivity is 1.33 (1.09), which corresponds to an error for the extracted conductivity anisotropy ±11 % (±3 %). Experimental comparison of the extracted transport anisotropy using two different contact sets (300 and 100 μm diameter) each on samples G100a1 and G100b yielded an agreement within 1–2% between the different contact sets, indicating negligible inhomogeneity of current injection underneath the contacts in these cases.

D. The three-dimensional conductivity tensor

Figure 5 schematically shows the monoclinic unit cell of β-Ga$_2$O$_3$ along with the unit basis vectors along a, b, c as well as unit vectors perpendicular to the lowest index planes along a^*, b^*, c^*. The vector representation of physical properties requires an orthonormal system. Two different systems abc^* and a^*bc have been chosen by different authors. We will use the a^*bc system by aligning the 1-axis along the (100) surface normal a^*, the 2-axis along b, and the 3-axis along the c axis, as indicated in Fig. 5. In this system, the conductivity tensor $\bar{\sigma}$ of β-Ga$_2$O$_3$, which relates electric field $\vec{E}$ and current density $\vec{j}$ by $\vec{j} = \bar{\sigma}\vec{E}$, can be expressed at zero magnetic field as [35]

$$\bar{\sigma} = \begin{pmatrix} \sigma_{a^*a^*} & 0 & \sigma_{a^*c} \\ 0 & \sigma_{bb} & 0 \\ \sigma_{a^*c} & 0 & \sigma_{cc} \end{pmatrix}, \tag{1}$$

where the off-diagonal elements both have the same value σ_{a^*c}. For isotropic materials, the conductivity tensor is a unity matrix times the scalar conductivity value. Different

values of the diagonal elements indicate different conductivity values along the axes of the coordinate system. Off-diagonal elements indicate a rotation between the axes of the coordinate system and the directions of minimum and maximum conductivity. Measurements using the van der Pauw configuration probe the conduction in the plane of the two-dimensional (2D) sample. In the following, we will derive the impact of the off-diagonal elements on 2D conductivity measurements in different sample orientations.

Rotation of the coordinate system

To use this derivation for differently oriented samples and a conductivity tensor defined in the a^*bc system, a rotation of the coordinate system to the system of the sample axes has to be done. The rotation of a tensor by the angle α around the b axis can be given as

$$\bar{\sigma}_{\text{rot}} = R_\alpha \bar{\sigma} R_\alpha^{-1}, \tag{2}$$

where the rotated conductivity tensor $\bar{\sigma}_{\text{rot}}$ follows a unitary transformation using the rotation matrix for a rotation around the b axis:

$$R_\alpha = \begin{pmatrix} \cos(\alpha) & 0 & \sin(\alpha) \\ 0 & 1 & 0 \\ -\sin(\alpha) & 0 & \cos(\alpha) \end{pmatrix}. \tag{3}$$

The transformation described by Eq. (2) can be derived by writing the relation $\vec{j} = \bar{\sigma}\vec{E}$ before and after applying a rotation,

$$\vec{j}_{\text{rot}} = R_\alpha \vec{j} = R_\alpha \bar{\sigma}\vec{E} = R_\alpha \bar{\sigma} R_\alpha^{-1} R_\alpha \vec{E} = \bar{\sigma}_{\text{rot}} \vec{E}_{\text{rot}}. \tag{4}$$

To rotate the coordinate system by a certain angle, both vectors and matrices have to be rotated by the negative value of that angle.

For samples having either one edge along the b axis or both edges within the ac plane, a corresponding Cartesian xbz system can be defined with the x axis either along the surface normal or along one sample edge, respectively. The corresponding tensor elements σ_{xx}, σ_{xz}, and σ_{zz} can be obtained by a rotation of the coordinate system around the b axis by the angle γ [described in Fig. 6(b)] from the a^*bc system to the system of the sample edges as follows:

$$\sigma_{xx} = \sigma_{a^*a^*}\cos^2\gamma - \sigma_{a^*c}\sin(2\gamma) + \sigma_{cc}\sin^2\gamma, \tag{5}$$

$$\sigma_{xz} = \sigma_{a^*c}\cos(2\gamma) + \tfrac{1}{2}(\sigma_{a^*a^*} - \sigma_{cc})\sin(2\gamma), \tag{6}$$

$$\sigma_{zz} = \sigma_{a^*a^*}\sin^2\gamma + \sigma_{a^*c}\sin(2\gamma) + \sigma_{cc}\cos^2\gamma, \tag{7}$$

where σ_{bb} is the same in both systems. For the a^*bc system, aligning $a^* = x$ and $z = c$ requires no further rotation. For the abc^* system, aligning a along x and z along c^*, the tensor elements in the a^*bc system can be obtained by a rotation of $\gamma = 13.7°$.

E. Calculation of the two-dimensional in-plane conductivity tensor

Using the general form of the conductivity tensor for a monoclinic material [Eq. (1)] in the Cartesian coordinate system of the sample edges with the 2-axis aligned
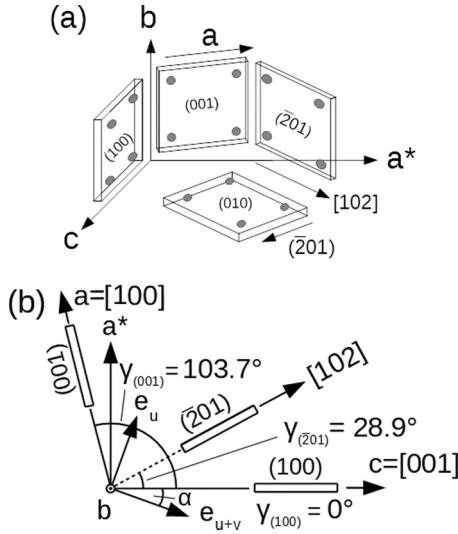
FIG. 6. (a) Overview of the orientation of the samples. Three samples have one edge along the b direction and the other edge is within the ac plane. (b) These three samples and the angles between them are shown in a projection onto the ac plane. This sketch includes the directions of minimum (u) and maximum ($u + v$) conductivity in the ac plane; α is the angle from these directions to the a^* and c axes. For each sample, γ is the angle from the c axis to the direction of the sample edge in the ac plane.

along b,

$$\bar{\sigma} = \begin{pmatrix} \sigma_{xx} & 0 & \sigma_{xz} \\ 0 & \sigma_{bb} & 0 \\ \sigma_{xz} & 0 & \sigma_{zz} \end{pmatrix}, \tag{8}$$

the relation $\vec{j} = \bar{\sigma}\vec{E}$ can be written as

$$\begin{pmatrix} j_x \\ j_b \\ j_z \end{pmatrix} = \bar{\sigma} \begin{pmatrix} E_x \\ E_b \\ E_z \end{pmatrix} = \begin{pmatrix} \sigma_{xx}E_x + \sigma_{xz}E_z \\ \sigma_{bb}E_b \\ \sigma_{xz}E_x + \sigma_{zz}E_z \end{pmatrix}. \tag{9}$$

For 2D samples with the surface normal along the x direction, one edge along the z direction in the a^*c plane, and the other edge along b, the condition of zero current perpendicular to the surface ($j_x = j_\perp = 0$) can be applied to Eq. (9),

$$0 = \sigma_{xx}E_x + \sigma_{xz}E_z, \tag{10}$$

which is equivalent to fixing the electric field perpendicular to the surface to

$$E_x = -\frac{\sigma_{xz}E_z}{\sigma_{xx}}. \tag{11}$$

Using Eqs. (9) and (11):

$$\begin{pmatrix} j_x \\ j_b \\ j_z \end{pmatrix} = \begin{pmatrix} \sigma_{xx}\left(-\frac{\sigma_{xz}E_z}{\sigma_{xx}}\right) + \sigma_{xz}E_z \\ \sigma_{bb}E_b \\ \sigma_{xz}\left(-\frac{\sigma_{xz}E_z}{\sigma_{xx}}\right) + \sigma_{zz}E_z \end{pmatrix}$$
$$= \begin{pmatrix} 0 \\ \sigma_{bb}E_b \\ \left(\sigma_{zz} - \frac{\sigma_{xz}^2}{\sigma_{xx}}\right)E_z \end{pmatrix}, \tag{12}$$

which can be rewritten to

$$\begin{pmatrix} j_x \\ j_b \\ j_z \end{pmatrix} = \begin{pmatrix} 0 & 0 & 0 \\ 0 & \sigma_{bb} & 0 \\ 0 & 0 & \sigma_{zz} - \frac{\sigma_{xz}^2}{\sigma_{xx}} \end{pmatrix} \begin{pmatrix} E_x \\ E_b \\ E_z \end{pmatrix}. \tag{13}$$

The 2D tensor in the coordinate system of the sample edges, the axes b and z, is now given by the bz components of the conductivity tensor in Eq. (13),

$$\bar{\sigma}^{bz} = \begin{pmatrix} \sigma_{bb} & 0 \\ 0 & \sigma_{zz} - \frac{\sigma_{xz}^2}{\sigma_{xx}} \end{pmatrix}. \tag{14}$$

The experimentally determined value of the conductivity anisotropy of one sample can now be given as the ratio of the diagonal elements in Eq. (14),

$$A_\sigma^{bz} = \frac{\sigma_{zz} - \frac{\sigma_{xz}^2}{\sigma_{xx}}}{\sigma_{bb}}. \tag{15}$$

1. (100) orientation

For (100)-surface samples ($=a^*$) with edges along [010]$=b$ and [001]$=c$, we can align these three directions along the x, y, and z axes, defining our Cartesian $xbz=a^*bc$ reference system. No further rotation is required and Eq. (15) can be rewritten as

$$A_\sigma^{(100)} = \frac{\sigma_{cc} - \frac{\sigma_{a^*c}^2}{\sigma_{a^*a^*}}}{\sigma_{bb}}. \tag{16}$$

2. (001) orientation

The (001)-surface samples ($=c^*$) have edges along [100]$=a$ and [010]$=b$. The angle from the c axis to the a axis is $\gamma_{(001)} = 103.7°$. Therefore, the (001) samples are rotated by an angle of $\gamma_{(001)} = 103.7°$ compared to the (100) samples around the b axis, as visualized in Fig. 6. So Eqs. (9) to (15) would be valid after a rotation of the coordinate system of $\gamma_{(001)} = 103.7°$.

Using this transformation [Eqs. (5) to (7)], the measured anisotropy for (001) samples can be described by Eq. (15) as well. This rotation is equivalent to the transformation from the a^*bc to the c^*ba system. Consequently, by aligning the x, y, and z axes along the directions c^*, b, and a, Eq. (15) can be expressed in the c^*ba system. As the conductivity is the same in c^* as in the $-c^*$ direction (using $\sigma_{c^*c^*} = \sigma_{(-c^*-c^*)}$), the tensor elements σ_{aa}, σ_{ac^*}, and $\sigma_{c^*c^*}$ are the same in the abc^* system and the c^*ba system:

$$A_\sigma^{(001)} = \frac{\sigma_{aa} - \frac{\sigma_{ac^*}^2}{\sigma_{c^*c^*}}}{\sigma_{bb}}. \tag{17}$$

3. ($\bar{2}\,0\,1$) orientation

The ($\bar{2}\,0\,1$)-surface samples have edges along [010]$=b$ and [102]. The angle from the c axis to the [102] direction is $\gamma_{(\bar{2}01)} = 28.9°$. The measured 2D anisotropy is given by Eq. (15), with the tensor elements rotated according to Eqs. (5) to (7) by the angle $\gamma_{(\bar{2}01)}$.

4. (010) orientation

For completeness, we are giving the transformation for (010)-surface samples with edges along [102] and ($\bar{2}$01) as well. As there is no off-diagonal conductivity tensor element perpendicular to the surface, the three-dimensional conductivity tensor from Eq. (8) can easily be rewritten to the 2D tensor,

$$\sigma^{zx} = \begin{pmatrix} \sigma_{zz} & \sigma_{xz} \\ \sigma_{xz} & \sigma_{xx} \end{pmatrix}. \tag{18}$$

To obtain the conductivity tensor elements in the *zx*-coordinate system of the sample edges, a rotation of the coordinate system of $28.9° = \gamma_{(\bar{2}01)}$ around the *b* axis according to Eqs. (5) to (7), where the [102] is aligned with the 1-axis (=*x*) and the ($\bar{2}$ 0 1) direction with the 3-axis (=*z*) of the 3D coordinate system. For the general case, 2D FEM simulations can be done using this conductivity tensor to obtain the relation to the measured transport anisotropy. A rotation of a multiple of 90° does not change the absolute value of the off-diagonal conductivity tensor elements [compare Eqs. (5) to (7)]. Therefore, the van der Pauw resistance anisotropy is independent of the value of the off-diagonal element for symmetric samples with no anisotropy in the diagonal elements. Our FEM simulations in the experimentally relevant range (off-diagonal values and deviations of the diagonal elements anisotropy from unity of less than 10% each) confirm the validity of the approximation $A_\sigma^{(010)} \approx \sigma_{xx}/\sigma_{zz}$ within an error of less than 0.05%.

F. Reconstructing the three-dimensional conductivity tensor

The 3D conductivity tensor has four independent elements [compare Eq. (1)]. Measurements of the 2D in-plane conductivity anisotropy of three differently oriented samples are thus sufficient to characterize the 3D conductivity anisotropy, as the tensor components can be normalized to one of the components. The (100), (001), and ($\bar{2}$01) surface samples all share one edge along the *b* direction and the other one in the *ac* plane [visualized in Fig. 6(a)]. Thus, their measured transport anisotropies [Eq. (15)] are ratios of *ac*-plane conductivities and σ_{bb}.

The 3D conductivity tensor given by Eq. (1) can be diagonalized by rotating the a^*bc coordinate system by an angle $-\alpha$ around the *b* axis into the $e_u b e_{u+v}$ coordinate system, whose axes are given by the directions e_u and e_{u+v} of minimum and maximum conductivity *u* and (*u* + *v*), respectively, in the *ac* plane, as illustrated in Fig. 6(b):

$$\sigma^{\text{min,max}} = \begin{pmatrix} u & 0 & 0 \\ 0 & \sigma_{bb} & 0 \\ 0 & 0 & u+v \end{pmatrix}. \tag{19}$$

Conversely, $\sigma^{\text{min,max}}$ can be expressed in the a^*bc system by a rotation of the $e_u b e_{u+v}$-system by α around the *b* axis, corresponding to a rotation of the tensor by $-\alpha$,

$$\sigma^{a^*bc} = \begin{pmatrix} \sigma_{a^*a^*} & 0 & \sigma_{a^*c} \\ 0 & \sigma_{bb} & 0 \\ \sigma_{a^*c} & 0 & \sigma_{cc} \end{pmatrix}$$

$$= \begin{pmatrix} u+v\sin^2\alpha & 0 & v\sin\alpha\cos\alpha \\ 0 & \sigma_{bb} & 0 \\ v\sin\alpha\cos\alpha & 0 & u+v\cos^2\alpha \end{pmatrix}. \tag{20}$$

Using the relation between the $e_u b e_{u+v}$ and the a^*bc coordinate system, the conductivity anisotropy for a (100) sample in Eq. (16) can be calculated using Eq. (20),

$$A_\sigma^{(100)} = \frac{u + v\cos^2\alpha - \frac{(v\sin\alpha\cos\alpha)^2}{u+v\sin^2\alpha}}{\sigma_{bb}}. \tag{21}$$

For the general case, a rotation of the angle $(\alpha + \gamma)$ instead of α has to be used,

$$A_\sigma^i = \frac{u + v}{\sigma_{bb}\left[1 + \frac{v}{u}\sin^2(\alpha + \gamma_i)\right]}, \tag{22}$$

where γ is the angle from the *c* axis to the direction of the sample edge in the *ac* plane for each sample [see Fig. 6(b)] and *i* denotes the surface orientation [e.g., (100), (001), and ($\bar{2}$01)]. This equation can be rewritten to a system of three coupled equations. As we are interested in conductivity anisotropies only, we can set the conductivity in the *b* direction $\sigma_{bb}=1$:

$$A_\sigma^{(100)}\left[1 + \frac{v}{u}\sin^2(\alpha + \gamma_{(100)})\right]\Big/(u+v) - 1 = 0, \tag{23}$$

$$A_\sigma^{(\bar{2}01)}\left[1 + \frac{v}{u}\sin^2(\alpha + \gamma_{(\bar{2}01)})\right]\Big/(u+v) - 1 = 0, \tag{24}$$

$$A_\sigma^{(001)}\left[1 + \frac{v}{u}\sin^2(\alpha + \gamma_{(001)})\right]\Big/(u+v) - 1 = 0, \tag{25}$$

with $\gamma_{(100)} = 0°$, $\gamma_{(\bar{2}01)} = 28.9°$, and $\gamma_{(001)} = 103.7°$.

For these three sample orientations, α, *u*, and *v* are the same and can thus be determined by solving the resulting system of the three coupled Eqs. (23) to (25) numerically using the experimentally measured A_σ^i. The conductivity tensor in the a^*bc system can then be readily calculated by Eq. (20).

III. RESULTS AND DISCUSSION

A. Room-temperature results

The measured value of the 2D conductivity anisotropy at room temperature, together with their relation to the three-dimensional conductivity tensor $\bar{\sigma}$ are summarized in Table V. For all samples, except G100c containing extended defects, a fairly isotropic in-plane conductivity was observed at room temperature with deviation of the conductivity anisotropy from unity of below 5%. Theory suggests a dependence of transport anisotropy on electron concentration or prevalent scattering mechanism (see Refs. [23,24] and Table I). We are thus using the data of samples G100a2, G001a2, and G-201a, which were prepared from the same Czochralski-grown boule and have similar electron concentrations (in the range of 2.5×10^{17} to 4.7×10^{17} cm^{-3}), to obtain the conductivity tensor given by Eq. (1) in the a^*bc reference system by solving the system of coupled Eqs. (23) to (25). The resulting tensor (normalized to the conductivity in the *b* direction) at room temperature is

$$\frac{\bar{\sigma}^{a^*bc}}{\sigma_{bb}}(T = 300 \text{ K}) = \begin{pmatrix} 1.01 \pm 0.04 & 0 & 0.05 \pm 0.03 \\ 0 & 1 & 0 \\ 0.05 \pm 0.03 & 0 & 0.96 \pm 0.01 \end{pmatrix}, \tag{26}$$

with the uncertainties based on those of the extracted 2D conductivity anisotropies in Table V of $\pm 1\%$, $\pm 3\%$, and

TABLE V. Values of the measured 2D conductivity anisotropy A at room temperature for different samples. The values were derived from comparing the measured van der Pauw anisotropy A_{vdP} to finite-element simulations (see Table III). As the off-diagonal element is much smaller than the diagonal elements, the given values are an approximation for the ratio of the conductivity along one side of the sample (c axis, a axis, [102]) and the other (b axis).

Sample name	2D anisotropy (3D tensor elements)	2D anisotropy value
G100a1 / a2	$\dfrac{\sigma_{cc} - \frac{\sigma_{a^*c}^2}{\sigma_{a^*a^*}}}{\sigma_{bb}}$	0.95 / 0.96
G100b	$\dfrac{\sigma_{cc} - \frac{\sigma_{a^*c}^2}{\sigma_{a^*a^*}}}{\sigma_{bb}}$	1.00
G100c (extended defects)	$\dfrac{\sigma_{cc} - \frac{\sigma_{a^*c}^2}{\sigma_{a^*a^*}}}{\sigma_{bb}}$	0.76
G001a1 / a2 /a3	$\dfrac{\sigma_{aa} - \frac{\sigma_{ac^*}^2}{\sigma_{c^*c^*}}}{\sigma_{bb}}$	1.02 / 0.99 / 0.95
G-201a / at1 /at2	$\dfrac{\sigma_{[102]} - \frac{\sigma_{[102](\bar{2}01)}^2}{\sigma_{(\bar{2}01)}}}{\sigma_{bb}}$	1.01 / 0.97 / 0.97
G-201bt	$\dfrac{\sigma_{[102]} - \frac{\sigma_{[102](\bar{2}01)}^2}{\sigma_{(\bar{2}01)}}}{\sigma_{bb}}$	1.00
G010at / bt	$\dfrac{\sigma_{[102][102]}}{\sigma_{(\bar{2}01)(\bar{2}01)}}$	1.03 / 1.07

$\pm3\%$ for G100a2, G001a2, and G-201a, respectively. Based on this tensor, the calculated 2D conductivity anisotropy $\sigma_{[102][102]}/\sigma_{(\bar{2}01)(\bar{2}01)} = 1.06$, using Eqs. (18) and (5) to (7), agrees well with the corresponding experimental value of 1.03 for the (010)-oriented UID sample G010at shown in Table V. Generally, our room-temperature results indicate a small anisotropy of the conductivity, with $\sigma_{a^*a^*}$ and σ_{cc} being a few % higher and lower than σ_{bb}, respectively, and the nondiagonal elements σ_{a^*c} amounting to no more than a few % of σ_{bb}. Due to the nonzero off-diagonal element, the actual direction of highest mobility in the a-c plane is $(59 \pm 15)°$ from the c direction towards the a^* direction with a conductivity $(1.12 \pm 0.09)\times$ that in the perpendicular direction of lowest conductivity. For comparison to other works using the abc^* reference system, we calculate the conductivity tensor in that system to be

$$\frac{\bar{\sigma}^{abc^*}}{\sigma_{bb}}(T = 300 \text{ K}) = \begin{pmatrix} 0.99 \pm 0.03 & 0 & 0.06 \pm 0.03 \\ 0 & 1 & 0 \\ 0.06 \pm 0.03 & 0 & 0.99 \pm 0.02 \end{pmatrix}.$$

(27)

To analyze the anisotropies of the scattering time, the conductivity tensor can be compared to an effective mass tensor. The tensor taken from [25], which Furthmüller *et al.* calculated by first principles, can be rotated to the a^*bc reference system and normalized to m^* along the b axis,

$$\frac{\bar{m}^*}{m_{bb}^*} = \begin{pmatrix} 1.009 & 0 & -0.001 \\ 0 & 1 & 0 \\ -0.001 & 0 & 0.973 \end{pmatrix}.$$

(28)

As the conductivity and the effective mass are close to isotropic, the overall scattering time at room temperature is
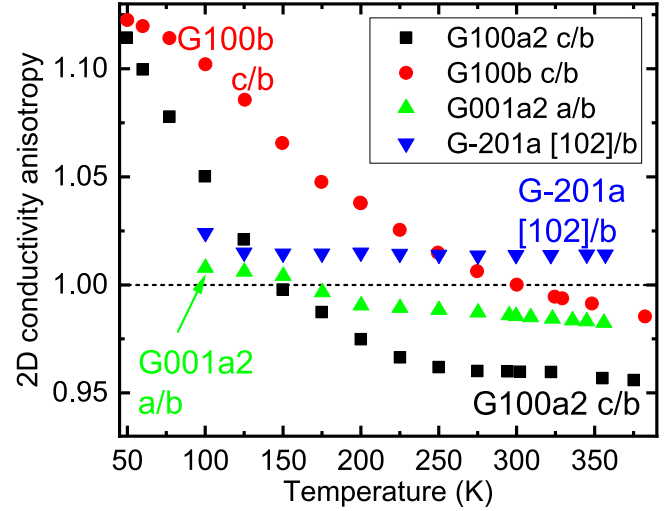

FIG. 7. Temperature-dependent 2D conductivity anisotropy A for representative samples with different surface orientations. The in-plane directions of the sample edges that result in the conductivity anisotropy, e.g., "c/b" resulting in $A = \sigma_{cc}/\sigma_{bb}$, are given with the sample name. The dashed line denotes completely isotropic in-plane conductivity.

quite isotropic as well. Using the relation $\bar{\sigma} = e^2 n \frac{\bar{\tau}}{m^*}$, the results from Eq. (26), and the effective mass tensor from [25], the τ tensor, normalized to τ_{bb}, can be calculated to be

$$\frac{\bar{\tau}}{\tau_{bb}} = \begin{pmatrix} 1.02 \pm 0.04 & 0 & 0.05 \pm 0.03 \\ 0 & 1 & 0 \\ 0.05 \pm 0.03 & 0 & 0.94 \pm 0.01 \end{pmatrix}$$

(29)

at room temperature, with $\tau_{a^*a^*}$ being $(9 \pm 5)\%$ higher than τ_{cc}.

B. Temperature dependence and scattering mechanisms

The temperature dependence between 50 and 380 K of measured 2D conductivity anisotropies A in the coordinate system of the sample edges is shown in Fig. 7 for a representative set of samples. (Note that the discussed changes of anisotropy with temperature for differently oriented samples is systematic as demonstrated for further samples with the same orientations in Fig. S1 in the Supplemental Material [36].)

A deviation of A from unity of less than 5% can be seen for temperatures between 175 and 380 K for all samples. These results suggest a rather isotropic conductivity at application-relevant (high) temperatures.

Between 380 and 100 K, the anisotropy of samples G001a2 and G-201a remains almost constant within 3% and 1%, respectively (0.98 to 1.01 and 1.02 to 1.02, respectively). In contrast, for the same temperature range, both G100a2 and G100b show a systematic increase of the anisotropy by $\approx10\%$ (0.96 to 1.05 and 0.99 to 1.10, respectively), which we attribute to a change of the dominant scattering mechanism as discussed next.

The electron mobility in β-Ga$_2$O$_3$ free from extended defects is mainly limited by polar longitudinal optical phonon scattering (PLOPS) and ionized-impurity scattering (IIS)
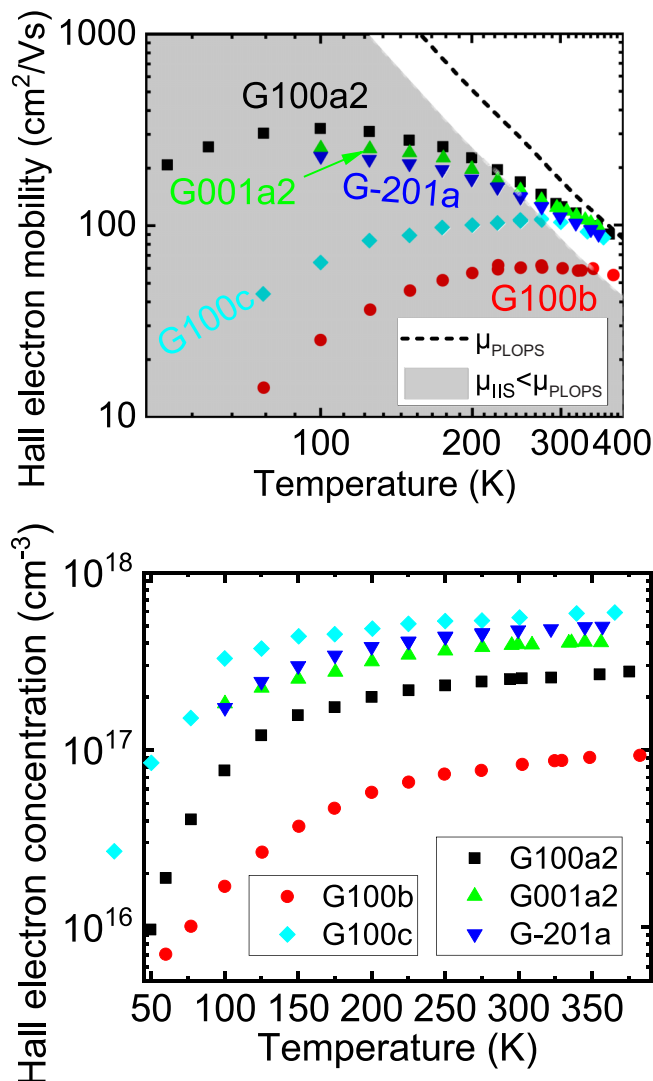
FIG. 8. Average Hall mobility (top) and electron concentration (bottom) as a function of temperature for various sample orientations. Measured values were corrected for the geometry effects of nonedge contact placement and finite contact size (see Table IV for correction factors). For comparison, we plot as broken line the PLOPS limit of mobility taken from Ref. [37] as well as the shaded region denoting a stronger IIS than PLOPS.

FIG. 9. Visualization of the temperature-dependent 3D conductivity tensor elements of β-Ga$_2$O$_3$ normalized to the conductivity in the b direction, σ_{bb}.

shaded region correspond to stronger IIS than PLOPS. Here, μ_{PLOPS} was taken from Ref. [37] describing β-Ga$_2$O$_3$ samples with the currently highest documented electron mobility. At temperatures below ≈ 250 K, all samples (Fig. 8, top) are dominated by IIS, whereas PLOPS is dominant for samples G100a2, G001a2, and G-201a at higher temperatures. As in the room-temperature case, the three latter samples, with similar electron mobility and concentration, are used to extract the temperature-dependent components of the conductivity tensor, shown in Fig. 9.

The tensor elements at temperatures above 250 K [including those at room temperature given in Eqs. (26) and (27)] represent dominant PLOPS. They are nearly isotropic ($\sigma_{cc}/\sigma_{bb} \approx 0.96$, $\sigma_{c^*c^*}/\sigma_{bb} \approx 0.99$, $\sigma_{aa}/\sigma_{bb} \approx 0.99$, and $\sigma_{a^*a^*}/\sigma_{bb} \approx 1.01$), in fair agreement with the theoretically predicted $\sigma_{c^*c^*}/\sigma_{bb} \approx 1.02$ of Ref. [23] as well as the experimentally determined $\sigma_{a^*a^*}/\sigma_{cc}$=1.10 to 1.15 of Ref. [21], both for dominant PLOPS and similar electron concentration to that of G100a2, G001a2, and G-201a. Our results, however, are significantly contrasting the theoretically predicted stronger anisotropy $\sigma_{c^*c^*}/\sigma_{bb} \approx 0.64$ of Ref. [24] and $\sigma_{aa}/\sigma_{bb} \approx 0.84$ of Ref. [23] as comparison to Eq. (27) yields.

Figure 9 further shows $\sigma_{cc}/\sigma_{bb} = 1.05$ and $\sigma_{a^*a^*}/\sigma_{bb} = 1.00$ at 100 K, where IIS is strongly dominating (cf. Fig. 8, top). These results indicate fairly isotropic IIS, but with higher σ_{cc}/σ_{bb} than in the case of PLOPS. Our experimental results are in agreement with the upper bound of 40% and 10% deviation from the isotropic case experimentally determined by optical Hall effect measurements of samples with IIS-dominated mobility at high donor concentration [22] and estimated theoretically for IIS [23], respectively, and give additional information on the directionality of the anisotropy.

Differently from the other representative samples, sample G100b is dominated by IIS at virtually all investigated temperatures (see Fig. 8, top). Comparing G100b (strong relative IIS) to G100a2 (weaker relative IIS), we find the anisotropy σ_{cc}/σ_{bb} to be systematically higher for G100b (see Fig. 7), reaching $\sigma_{cc}/\sigma_{bb} \approx 1.10$ at 100 K. In qualitative

at fixed ionized point charges [23,28,37]. With increasing temperature, the electron mobility limited by PLOPS (μ_{PLOPS}) or IIS (μ_{IIS}) decreases or increases, respectively, and higher ionized point charge concentrations (including dopants, compensating dopants, or point defects) decrease the IIS-limited mobility [28]. Figure 8 shows the temperature-dependent Hall electron mobility and Hall electron concentration of the representative set of samples. (The corresponding data for all investigated samples are shown in the Supplemental Material [36].) To identify the dominant scattering mechanisms (PLOPS or IIS) for all samples, we compare the measured temperature-dependent mobilities μ to the case of $\mu_{\text{PLOPS}} = \mu_{\text{IIS}}$, i.e., $\mu = 1/(1/\mu_{\text{PLOPS}} + 1/\mu_{\text{IIS}}) = \mu_{\text{PLOPS}}/2$ by Matthiessen's rule, drawn as the boundary between the shaded and white region in the top panel of Fig. 8. Data points in the
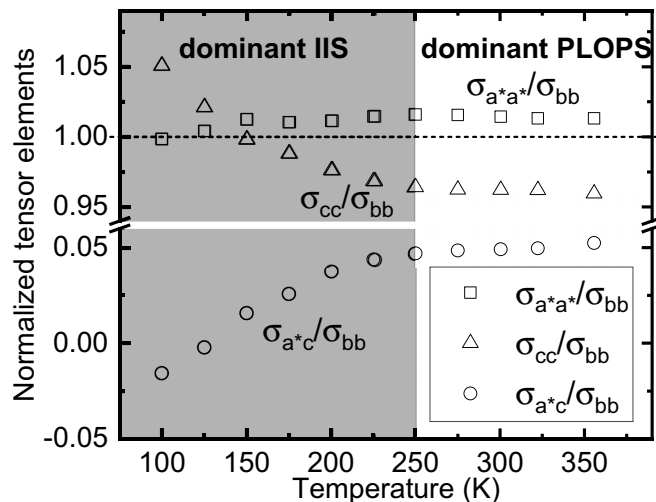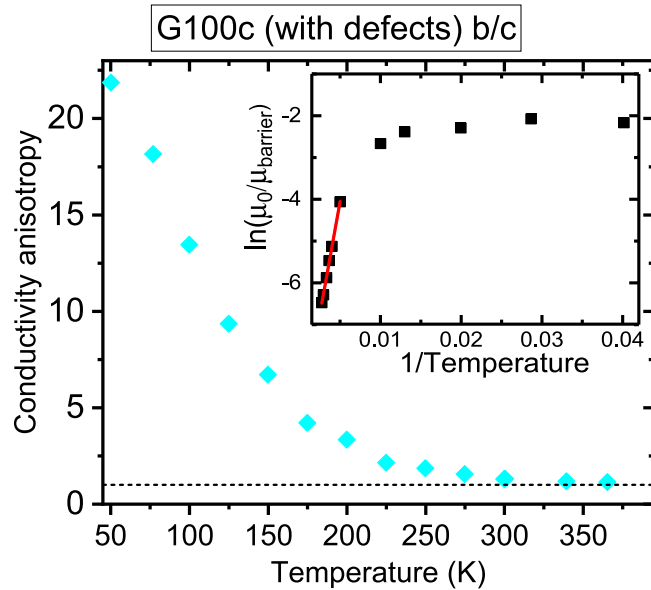
FIG. 10. Conductivity anisotropy of sample G100c containing low-angle grain boundaries along the *b* direction. The dashed line denotes completely isotropic in-plane conductivity. The inset shows an Arrhenius plot of the barrier-related mobility [compare Eq. (31); the fit between 200 and 365 K results in an activation energy of 93 ± 5 meV].

agreement with an increase of σ_{cc}/σ_{bb} for G100a2 with decreasing temperature, this result corroborates systematically higher σ_{cc}/σ_{bb} for dominant IIS than for dominant PLOPS. This systematically higher IIS-dominated conductivity in the *c* direction compared to the almost equal conductivities in the *a* and *b* directions is likely related to the higher dielectric constant (of 12.4) for the *c* direction compared to the almost equal dielectric constants (of 10.2 and 10.9) for directions perpendicular to *c* [15,16].

C. Anisotropy by extended defects

Large conductivity anisotropies with significantly higher conductivity in the *b* than in the *c* direction have been identified in sample G100c, which contains low-angle grain boundaries oriented approximately along the *b* direction (see Figs. 2 and 3). In this sample, the room-temperature conductivity anisotropy $\sigma_{cc}/\sigma_{bb} \approx 0.77$ (shown in Table V) is much stronger than that of the comparable high-quality samples G100a1, G100a2, and G100b. A qualitatively similar behavior with $\sigma_{cc}/\sigma_{bb} \approx 0.06$ and $\sigma_{cc}/\sigma_{bb} \approx 0.5$ at room temperature has been observed in β-Ga$_2$O$_3$ (100) bulk samples of unknown structural quality [10] and layers containing a high density of incoherent twin boundaries oriented along the *b* direction [19], respectively. Planar defects, such as twin or grain boundaries, are typically associated with energy barriers that impede electron transport across the defects, explaining the relatively lower conductivity along the *c* direction for G100c [38,39]. For convenience, we plot the temperature dependence of the inverse anisotropy, σ_{bb}/σ_{cc}, for sample G100c in Fig. 10. A strong increase of anisotropy with decreasing temperature from $\sigma_{bb}/\sigma_{cc} = 1.14$ at $T = 360$ K to $\sigma_{bb}/\sigma_{cc} > 20$ at $T = 50$ K is observed. (We note that the
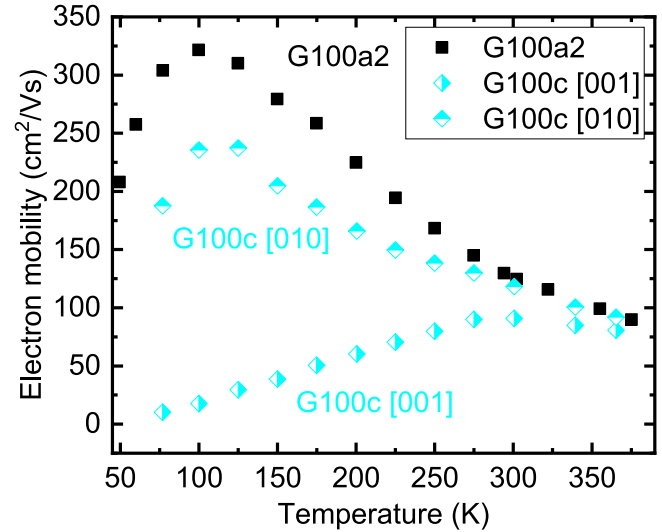

FIG. 11. Temperature-dependent Hall mobility for sample G100c containing low-angle grain boundaries along the *b* direction. Cyan rhombs: mobility along ([010]) and perpendicular to ([001]) the grain boundaries. Black squares: mobility of a similar sample without these defects (G100a2) for comparison.

increasing anisotropy σ_{cc}/σ_{bb} with decreasing temperature in samples G100a1, G100a2, and G100b cannot be related to such extended defects as it is inverse to the increasing σ_{bb}/σ_{cc} of G100c.) Figure 11 shows the mobility in the direction parallel and perpendicular to the low-angle grain boundary defects in sample G100c. Parallel to the defects, the mobility is similar to that of a comparable sample without these defects, G100a2, whereas it is drastically reduced perpendicular to the defects, especially at low temperatures. Above room temperature, however, the mobilities in both directions coincide and decrease with increasing temperature as expected for phonon-limited transport, indicating a negligible effect of the grain boundaries. Assuming the mobility μ within the grains to be isotropic, the total mobility perpendicular to the defects ([001] direction), $\mu_\perp$, is reduced due to the activated, barrier-related mobility μ_{barrier},

$$\frac{1}{\mu_\perp} = \frac{1}{\mu} + \frac{1}{\mu_{\text{barrier}}}. \tag{30}$$

As $A_\sigma \approx \frac{\sigma_{bb}}{\sigma_{cc}} \approx \mu/\mu_\perp$,

$$\mu_{\text{barrier}} = \frac{\mu}{A_\sigma - 1} = \mu_0 e^{\frac{E_a}{kT}}, \tag{31}$$

using this equation, the activation energy for the transport across the barriers is $E_A = (93 \pm 5)$ meV for temperatures between 200 and 365 K (see inset of Fig. 10). Interestingly, this barrier is orders of magnitude higher than that found at low-angle grain boundaries of bulk SnO$_2$ [34], which might also explain the difficulties in realizing conductive, nonsingle-crystalline β-Ga$_2$O$_3$ films with grain or (rotational) domain boundaries.

IV. SUMMARY AND CONCLUSION

Using van der Pauw measurements with well-defined contact geometry and FEM modeling of the structures, the

anisotropy of the electrical conductivity in high-quality bulk β-Ga$_2$O$_3$ wafers with different surface orientation was precisely determined.

Most importantly, fairly isotropic behavior with conductivity ratios of less than 1.10 along different low-index directions at temperatures between 100 and 380 K was found at electron concentrations of the order of 3×10^{17} cm^{-3}. Based on the extracted anisotropies, the ratio of the nonzero elements of the conductivity tensor was determined and the off-diagonal element was found to be no more than $(5 \pm 3)\%$ of the diagonal ones. A consequence relevant for optimum performance of transport-based electronic devices, such as transistors, is the direction of highest mobility, which is rotated $(59 \pm 15)°$ from the c direction towards the a^* direction in the a-c plane.

Conductivity anisotropies well in excess of 10%, as reported in Refs. [10,20], are likely not intrinsic, but rather related to experimental artifacts or extrinsic causes, such as extended structural defects (incoherent twin boundaries [19] or grain boundaries). To this end, we experimentally demonstrated that high anisotropies can indeed be caused by oriented low-angle grain boundaries whose barriers were found to be up to 93 meV high. Therefore, we suggest to use the in-plane conductivity anisotropy of a bulk or thin-film sample, e.g., measured by the experimentally straightforward van der Pauw method, as a quality indicator for extended defects oriented along an in-plane direction.

Comparison to the slightly anisotropic effective mass tensor indicates that the intrinsic transport anisotropy is strongly influenced by the scattering times of anisotropic scattering mechanisms. Inspection of the temperature-dependent electron mobility between 100 and 380 K allowed us to distinguish dominant polar longitudinal optical-phonon scattering (PLOPS) from dominant ionized-impurity scattering (IIS): Irrespective of scattering mechanism, the conductivities in the a and b directions agree within 2%. The ratio of the conductivities along the c and b directions, however, is 0.96 ± 0.01 for PLOPS and increases up to 1.12 for IIS. We tentatively relate the $a - b$ isotropy and $c - b$ anisotropy of IIS to the corresponding anisotropy of the dielectric constant of β-Ga$_2$O$_3$ [15,16]. Most of the conductivity anisotropies predicted by first-principles theory [23,24] are significantly larger than those experimentally found in this work. Their predicted dependence on electron concentration [23,24] motivates further experimental investigation of the transport anisotropy at higher electron concentrations (e.g., above 10^{19} cm^{-3}).

[1] M. Higashiwaki, A. Kuramata, H. Murakami, and Y. Kumagai, J. Phys. D **50**, 333002 (2017).

[2] M. Higashiwaki and G. H. Jessen, Appl. Phys. Lett. **112**, 060401 (2018).

[3] T. Oshima, T. Okuno, and S. Fujita, Jpn. J. Appl. Phys. **46**, 7217 (2007).

[4] U. Lampe, M. Fleischer, and H. Meixner, Sens. Actuators B: Chemical **17**, 187 (1994).

[5] S. Geller, J. Chem. Phys. **33**, 676 (1960).

[6] Z. Guo, A. Verma, X. Wu, F. Sun, A. Hickman, T. Masui, A. Kuramata, M. Higashiwaki, D. Jena, and T. Luo, Appl. Phys. Lett. **106**, 111909 (2015).

[7] M. D. Santia, N. Tandon, and J. D. Albrecht, Appl. Phys. Lett. **107**, 041907 (2015).

[8] M. Handwerg, R. Mitdank, Z. Galazka, and S. F. Fischer, Semicond. Sci. Technol. **31**, 125006 (2016).

[9] C. Sturm, J. Furthmüller, F. Bechstedt, R. Schmidt-Grund, and M. Grundmann, APL Mater. **3**, 106106 (2015).

[10] N. Ueda, H. Hosono, R. Waseda, and H. Kawazoe, Appl. Phys. Lett. **71**, 933 (1997).

[11] T. Onuma, S. Saito, K. Sasaki, T. Masui, T. Yamaguchi, T. Honda, and M. Higashiwaki, Jpn. J. Appl. Phys. **54**, 112601 (2015).

[12] H. He, R. Orlando, M. A. Blanco, R. Pandey, E. Amzallag, I. Baraille, and M. Rérat, Phys. Rev. B **74**, 195123 (2006).

[13] B. Liu, M. Gu, and X. Liu, Appl. Phys. Lett. **91**, 172102 (2007).

[14] M. Schubert, R. Korlacki, S. Knight, T. Hofmann, S. Schöche, V. Darakchieva, E. Janzén, B. Monemar, D. Gogova, Q.-T. Thieu *et al.*, Phys. Rev. B **93**, 125209 (2016).

[15] A. Fiedler, R. Schewski, Z. Galazka, and K. Irmscher, ECS J. Solid State Sci. Technol. **8**, Q3083 (2019).

[16] K. Ghosh and U. Singisetti, Appl. Phys. Lett. **109**, 072102 (2016).

[17] K. Irmscher, Z. Galazka, M. Pietsch, R. Uecker, and R. Fornari, J. Appl. Phys. **110**, 063720 (2011).

[18] O. Bierwagen, R. Pomraenke, S. Eilers, and W. T. Masselink, Phys. Rev. B **70**, 165307 (2004).

[19] A. Fiedler, R. Schewski, M. Baldini, Z. Galazka, G. Wagner, M. Albrecht, and K. Irmscher, J. Appl. Phys. **122**, 165701 (2017).

[20] E. G. Villora, K. Shimamura, Y. Yoshikawa, K. Aoki, and N. Ichinose, J. Cryst. Growth **270**, 420 (2004).

[21] M. H. Wong, K. Sasaki, A. Kuramata, S. Yamakoshi, and M. Higashiwaki, Jpn. J. Appl. Phys. **55**, 1202B9 (2016).

[22] S. Knight, A. Mock, R. Korlacki, V. Darakchieva, B. Monemar, Y. Kumagai, K. Goto, M. Higashiwaki, and M. Schubert, Appl. Phys. Lett. **112**, 012103 (2018).

[23] Y. Kang, K. Krishnaswamy, H. Peelaers, and C. G. V. de Walle, J. Phys.: Condens. Matter **29**, 234001 (2017).

[24] K. Ghosh and U. Singisetti, J. Mater. Res. **32**, 4142 (2017).

[25] J. Furthmüller and F. Bechstedt, Phys. Rev. B **93**, 115204 (2016).

[26] H. Peelaers and C. G. Van de Walle, Phys. Status Solidi B **252**, 828 (2015).

[27] K. Yamaguchi, Solide State Commun. **131**, 739 (2004).

[28] N. Ma, N. Tanen, A. Verma, Z. Guo, T. Luo, H. G. Xing, and D. Jena, Appl. Phys. Lett. **109**, 212101 (2016).

[29] Z. Galazka, K. Irmscher, R. Uecker, R. Bertram, M. Pietsch, A. Kwasniewski, M. Naumann, T. Schulz,

R. Schewski, D. Klimm *et al.*, J. Cryst. Growth **404**, 184 (2014).

[30] Z. Galazka, R. Uecker, D. Klimm, K. Irmscher, M. Naumann, M. Pietsch, A. Kwasniewski, R. Bertram, S. Ganschow, and M. Bickermann, ECS J. Solid State Sci. Technol. **6**, Q3007 (2017).

[31] A. Kuramata, K. Koshi, S. Watanabe, Y. Yamaoka, T. Masui, and S. Yamakoshi, Jpn. J. Appl. Phys. **55**, 1202A2 (2016).

[32] C. Gao, O. Brandt, S. C. Erwin, J. Lahnemann, U. Jahn, B. Jenichen, and H.-P. Schonherr, Phys. Rev. B **82**, 125415 (2010).

[33] A. J. Wilkinson, G. Meaden, and D. J. Dingley, Mater. Sci. Technol. **22**, 1271 (2006).

[34] O. Bierwagen and Z. Galazka, Appl. Phys. Lett. **112**, 092105 (2018).

[35] A. Parisini and R. Fornari, Semicond. Sci. Technol. **31**, 035023 (2016).

[36] See Supplemental Material at http://link.aps.org/supplemental/10.1103/PhysRevMaterials.3.124604 for the temperature-dependent transport data of all measured samples.

[37] Y. Zhang, F. Alema, A. Mauze, O. S. Koksaldi, R. Miller, A. Osinsky, and J. S. Speck, APL Mater. **7**, 022506 (2019).

[38] J. Y. W. Seto, J. Appl. Phys. **46**, 5247 (1975).

[39] J. W. Orton and M. J. Powell, Rep. Prog. Phys. **43**, 1263 (1980).